Spectral Mixture Analysis as a Unified Framework for the Remote Sensing of Evapotranspiration

Daniel Sousa [1,*] and Christopher Small[1]

[1] Lamont-Doherty Earth Observatory, Columbia University
* Correspondence: d.sousa@columbia.edu; Tel.: +1-530-304-4992

Received: October 24, 2018; Accepted: date; Published: date

Abstract: This analysis proposes a unified framework for estimation of evapotranspiration (ET) using spectral mixture analysis (SMA) based on globally standardized substrate, vegetation, and dark (SVD) endmembers (EMs). Using all available Landsat 8 scenes from a month in the peak growing season (June) in a diverse 90 x 120 km region in northern California, we characterize the relationship between each of the S, V, D land cover fractions versus apparent brightness temperature (T), as well as ET fraction (EF) and moisture availability (Mo) estimated using the Triangle Method [1,2]. V fraction yields accurate, linearly scalable estimates of subpixel vegetation abundance which contain considerably more structure than either the linearly or quadratically normalized spectral indices that are generally used in ET studies. D fraction yields information which is very similar to shortwave broadband albedo. S fraction estimates, at least for this geographic area and season, show a consistent ($\rho \sim 0.7$ to 0.9) linear relationship to T. Because the SVD approach includes accurate, scalable estimates of both vegetation abundance and albedo, it provides a physically-based conceptual framework that unifies the two most widely used approaches to estimation of ET from remotely sensed observations. The additional information provided by the third (S) fraction is suggestive of a potential avenue for ET model improvement by providing an explicit observational constraint on the exposed soil fraction. Taken together, these results suggest the potential for a single unified framework for ET estimation. The strong linear scaling properties of SMA fraction estimates from meter to kilometer scales also facilitate vicarious validation of ET estimates using multiple resolutions of imagery.

Keywords: Spectral Mixture Analysis; Evapotranspiration; Surface Energy Balance

---

1. Introduction

Earth's lithosphere, atmosphere, and biosphere are unified by the movement of water. Evapotranspiration (ET; the sum of evaporation and transpiration) is a central mechanism in this exchange. Accordingly, ET plays a major role in Earth's surface energy balance and global biogeochemical cycles. Global distributions of the components of ET [3], as well as multidecadal trends [4] are of broad interest to a wide range of scientific communities. ET is an integral part of the climate system, with clear global teleconnections between ET and phenomena like the El Niño-Southern Oscillation [5], as well as direct relationships between soil moisture and temperature [6].

In addition to its importance for understanding fundamental Earth system processes, ET also has clear practical applications. ET has long been recognized as practical indicator of plant water stress [7–9]. In agricultural settings, near real-time ET monitoring can improve predictions of irrigation need and regulatory estimates of water use. In natural environments, ET can inform studies of ecosystem health and biodiversity. For recent reviews of the potential applications of ET monitoring, as well as outstanding unresolved questions, see [10] and [11].

Despite its centrality to such a wide range of fundamental Earth systems, accurate and consistent estimation of ET remains a challenge. For instance, a recent analysis found that over 50 models currently exist to compute potential ET, and that model choice can impact flux estimates by over 25% [12]. Uncertainty in ET estimation has substantial implications for our ability to manage agriculture and monitor wildlands, as well as for our understanding of deeper questions about the Earth system such as the amplitude of global water and energy fluxes. This uncertainty is, at least in part, a result of differences in the data streams, underlying assumptions, and conceptual approaches used by each model. The more that these disparities can be integrated into a single framework, the more it will be possible to reduce the overall uncertainty in ET estimation.

Algorithms that estimate ET on landscape scales generally rely on observations from optical and thermal remote sensing. The ET model parameters that remote sensing observations are most commonly used to constrain are fractional vegetation cover (V), surface temperature (T), and albedo (α). The relationships among these three quantities can be understood in the context of their bivariate distributions. The distribution of V vs T gives information about plant-based evapotranspirative cooling and is fundamental to the physical basis of many popular ET models (e.g. [13–16]). The distribution of α vs T has also been long recognized [17], and provides information about soil moisture ([18,19]) and roughness [20]. α vs T has been incorporated into a popular ET model by [21]. Recent work by [22] has developed a model based on fusion of both the V vs T and α vs T relationships, with encouraging results.

For the vast majority of current ET estimation algorithms and associated Surface-Vegetation-Atmosphere Transfer (SVAT) models, vegetation abundance is computed with a spectral index. The specific index used varies from model to model. Many models (e.g. [23,24]) rely directly upon the Normalized Difference Vegetation Index (NDVI). However, all spectral indices use only a small subset of the information present in multispectral imagery. NDVI in particular has a number of known flaws, including scaling nonlinearities ([2,25,26]), sensitivity to both soil background and atmospheric effects ([27,28]), and saturation effects over a wide range of vegetation fractions [28]. In response to these problems, NDVI is often normalized using linear (e.g. [29]) or quadratic (e.g. [30–32]) transformations. Each spectral index, transformed or untransformed, gives different estimates of vegetation abundance, which then result in differences in estimated ET. If these metrics could be improved and standardized, ET models could be made more accurate and cross-model standardization could be more effective.

Spectral Mixture Analysis (SMA; [33–35]) is a physically-based method that uses the full reflectance spectrum, rather than a small subset of bands, to estimate V. SMA-based estimates of V mitigate many of the problems with spectral indices. SMA explicitly accounts for illumination effects as well the reflectance of the soil & NPV background, substantially improving estimates at low vegetation abundance [27]. Because SMA relies on area-weighted linear mixing of radiance from materials within the pixel, V estimates are relatively insensitive to sensor spatial resolution and have been shown to scale linearly from 2 m to 30 m ([26,28]) as well as from meter-scale field measurements [25]. This simple linear scaling could be a key advantage for ET studies, given the widely recognized scaling nonlinearities of ET estimates (e.g. [36–41]). SMA fraction estimates are sensitive to the spectra of the endmember (EM) materials, but previous work has characterized the global multispectral mixing space and proposed generic EMs which well-describe the majority of the Earth’s land environments and are calibrated across sensors ([28,42,43]).

In addition to providing enhanced estimates of V, SMA simultaneously provides accurate estimates of two additional physically meaningful quantities: 1) the areal abundances of soil, rock and NPV Substrates (S), and 2) Dark features (D) such as shadow, water, and low-albedo surfaces. These estimates are made at subpixel resolution and with trivial computational cost. D fraction estimates represent the effects of albedo (α), illumination geometry, atmospheric opacity, and soil moisture content, thereby modulating the overall amplitude of the reflectance signal. S fraction estimates provide information about the compositional properties of the soil and NPV substrate background at each pixel. To our knowledge, SMA has not yet been used in ET estimation algorithms. This could represent a missed opportunity. When compared against coincident T measurements, SVD fractions can provide a unifying framework which incorporates two major existing approaches to ET estimation (V vs T and α vs T), and also includes a novel, potentially useful supplement (S vs T).

The primary purpose of this analysis is to explore the SVD model as an innovative conceptual framework for ET estimation. We illustrate the relationships between each fraction and T, as well as ET Fraction (EF) and Moisture Availability (Mo) estimates derived using the popular Triangle method. We use all available Landsat 8 acquisitions from the peak growing season (June) in a 120 x 90 km region of northern California with broad vegetation and soil diversity. For every image examined, we find that V better represents the variability in vegetation present in the study area than NDVI* or NDVI*^{2}. In contrast, D captures very similar information to (inverted) overall shortwave albedo estimates. Most surprisingly, S yields a strong ($\rho \sim 0.7$ to 0.9) linear relationship with T for every image we examine. The results of this analysis suggest that SMA has the potential to improve the accuracy and consistency of ET estimates, inform flux partitioning, and provide a unifying approach for complementary use of multispectral optical and thermal imagery.

1.1. ET Model Overview

1.1.1. Models relying on V vs T

Extensive previous work has been published regarding the combined use of optical and thermal imagery for ET monitoring. A plethora of physical and statistical models have been built to approach the problem. One of the first approaches ([1,2] and subsequent publications; reviewed by [30]) was based on the observed triangular (or trapezoidal, [16]) relationship for many landscapes in the vegetation index vs temperature space. The physical basis for this triangular relationship is the evapotranspirative cooling which occurs in dense well-watered vegetation, and which may or may not occur in unvegetated areas depending on moisture availability.

Other popular approaches, such as SEBAL [14] and METRIC [13] are primarily based on the information contained in spatial variability of the temperature field across a landscape. Another class of approaches, most notably the ALEXI/DisALEXI model ([44–46]) rely on time differencing of the thermal field to capture variations in the diurnal temporal trajectory of different land covers. Despite their different sets of assumptions and governing equations, all these models generally require vegetation abundance estimates, and rely on spectral indices to provide them.

1.1.2. Models relying on α vs T

Early work based in north Africa observed a strong relationship between overall surface reflectance (albedo) and ET [17]. This relationship was interpreted in the context of the surface energy balance equations. Four models were presented which could potentially describe the physical meaning of the relationship. These were later brought into a formal surface energy balance model by [21]. This model decomposes the relationship in α vs T space into evaporation-controlled and radiation-controlled regimes. The evaporation-controlled regime is active at lower albedos and is characterized by an increase in T with increasing α, physically explained by moisture darkening of soils. Once the soils are sufficiently dry for the effects of moisture darkening to become negligible, the sign of the relation reverses and T decreases with increasing α. The physical explanation for this is the decreased absorption of incident radiation at higher albedos. Comparative studies of the α and T and V vs T relations (e.g. [47,48]) can provide insight into the relative strength of the physical processes underlying each conceptual framework. More recently, [22] have developed an integrated approach which unites the V vs T and α vs T relations into a single model.

The above summary of models is not intended to be comprehensive. Rather, it is designed to present the reader with a sampling of the range of ET estimation methods extant in the literature and to show the ways in which V, α and T are incorporated into ET estimation algorithms. For more comprehensive reviews of these methods (and more), see [49–51].

1.2. Spectral Mixture Analysis

Multispectral satellite imaging sensors generally measure reflectance in 4 to 12 optical wavelength intervals. Vegetation indices are generally based on only 2 or 3 of these wavelengths, leveraging the distinctive visible-NIR "red edge" that makes vegetation abundance one of the strongest signals present in multispectral data. The information present in the surface reflectance at other visible and IR wavelengths, unused by spectral indices, can provide significantly more information than vegetation abundance alone. SMA [33–35] is a well-established, physically-based way to retrieve this additional information.

SMA assumes area-weighted linear mixing of upwelling radiance within the IFOV of each multispectral pixel. While not always a valid assumption, linear mixing has been shown by [52–54] to have solid theoretical and observational basis for practical application. SMA treats each pixel spectrum as a linear combination of pure EM spectra and inverts a set of linear mixing equations to accurately estimate the subpixel abundance of each EM material.

Theoretically, as many materials could be mapped as wavelengths measured by the multispectral imager (4 to 12). In practice, however, 6-band Landsat spectra have been shown to essentially represent only 3 distinct land cover types on ice-free land surfaces ([42,55]) corresponding to Substrate, Vegetation, and Dark surfaces (S, V, and D). Similar EMs emerge from diverse mixing spaces of higher dimensional 12-band Sentinel-2 imagery [56], and 224-band hyperspectral AVIRIS flight line composites [57]. These studies suggest that an approach based on estimation of 3 materials from multispectral imagery is likely to be generally applicable across most terrestrial surfaces relevant to ET analysis.

Reflectance spectra of the 3 global SVD EMs for Landsat 8 OLI are shown in Figure 1. S fractions represent materials such as soil, rock, and non-photosynthetic vegetation. V fractions represent illuminated photosynthetic vegetation. D fractions can variously represent shadow, water, or low albedo surfaces such as mafic rocks and some impervious surfaces. The spectral mixing space spanned by the bounding S, V, and D EMs includes the full range of subpixel mixtures of rock and soil substrates and different classes of vegetation with varying structural shadow and illumination conditions, as well as substrate and vegetation types with distinct lower amplitude reflectances. Snow, ice, evaporate materials and shallow marine substrates occupy distinct limbs of the global mixing space, but are generally not considered in ET studies and will not be discussed in this analysis.

2. Materials and Methods

2.1. Data

This analysis relies on optical data from the Operational Land Imager (OLI) and thermal data from the Thermal Infrared Sensor (TIRS) instruments onboard Landsat 8. Landsat data were downloaded free of charge as DNs from the USGS GloVis download hub (http://glovis.usgs.gov). Optical and thermal image data were calibrated to exoatmospheric reflectance and apparent brightness temperature, respectively, using the standard calibration procedures described in the Landsat Data Users Handbook [58]. All data were downloaded with Collection 1 preprocessing, which incorporates the standard correction [59] to the well-known TIRS stray light problem [60]. No atmospheric correction was attempted. Where indicated, 30 m OLI bands were convolved with a 21 x 21 low pass Gaussian kernel to simulate the larger 100 m IFOV of the TIRS.

2.2. Normalizations

Evapotranspiration Fraction (EF) and Moisture Availability (Mo) were estimated using the generalized Triangle method coefficients proposed by [30]. This approach was chosen because of its simplicity and popularity. Apparent brightness temperature was normalized to T* using the linear transformation suggested in [30]:

$$T^* = \frac{T - T_{min}}{T_{max} - T_{min}}$$

The values of T_{min} and T_{max} used for all scenes were 285 K and 335 K, respectively. While ET estimates could be more accurate if scene-to-scene differences in air temperature were accounted for by using scene-specific T_{min} and T_{max} values, we use global values to facilitate intercomparison between scenes.

NDVI was computed using the standard relation:

$$NDVI = \frac{NIR - Red}{NIR + Red}$$

Linearly transformed NDVI* was computed using the relation popularized by [61]:

$$NDVI^* = \frac{NDVI - NDVI_{min}}{NDVI_{max} - NDVI_{min}}$$

Quadratically transformed $NDVI^{*2}$ was computed using the relation suggested by [30]:

$$NDVI^{*2} = \left(\frac{NDVI - NDVI_{min}}{NDVI_{max} - NDVI_{min}}\right)^2$$

$NDVI_{max}$ and $NDVI_{min}$ values were identified to be 0.85 and 0.15, respectively, for all scenes. Albedo calculations are performed using the shortwave broadband albedo coefficients from [62].

2.3. Study Area

The study area used for this analysis is a 120 x 90 km region comprising the Sacramento Valley of California and its surrounding foothills. The region hosts a broad diversity of soils and vegetation types. The valley is flat and dominated by high intensity agriculture. Rice is commonly grown in the clay-rich soils away from the Sacramento and Feather River channels. A diverse mix of row crops and orchards is grown in the sandier soils closer to the river channels and valley edges. The foothills of the Coast Ranges (west of the valley), Sierra Nevada (east of the valley) and Sutter Buttes (center of the valley) provide topographic relief and are generally covered with mixed rainfed grasslands which are predominantly used for grazing. The northeast and southwest corners of the scene capture coniferous and deciduous forests which are common at higher elevations surrounding the study area. Spatially extensive human settlements are present in the southeast (Sacramento/Davis/Woodland) and central east (Marysville/Yuba City) portions of the scene. The deep reservoirs of Lake Berryessa (southwest corner) and Lake Oroville (northeast corner) are also present. The climate of the region is classified as Hot Summer Mediterranean (Köppen *Csa*), with hot, dry summers and cool, wet winters.

Figure 1 shows the region as imaged by Landsat 8 on June 19, 2013. The natural color composite image (upper left) allows for broad discrimination between the foothill grasslands, valley agriculture, and upland forests. However, substantially more information is provided by the infrared bands shown in the false color composite (upper right). Here, substantial diversity is apparent in soil and NPV background reflectance, as well as enhanced discrimination between flooded rice fields (black) and non-flooded row and orchard crops (green/brown/red). The SVD fraction image (lower left) shows the physically-relevant subpixel areal abundance information which is extracted from the multispectral reflectance data by SMA using the inset globally standardized EMs from [43]. Vegetation indices provide an approximation of only the green channel of this image. The red channel of this image (S fraction abundance) shows substantial visual similarity to hot (red) values recorded by the thermal image (lower right). The similarity between these two spatial patterns provides qualitative visual evidence suggesting a strong S vs T relationship.

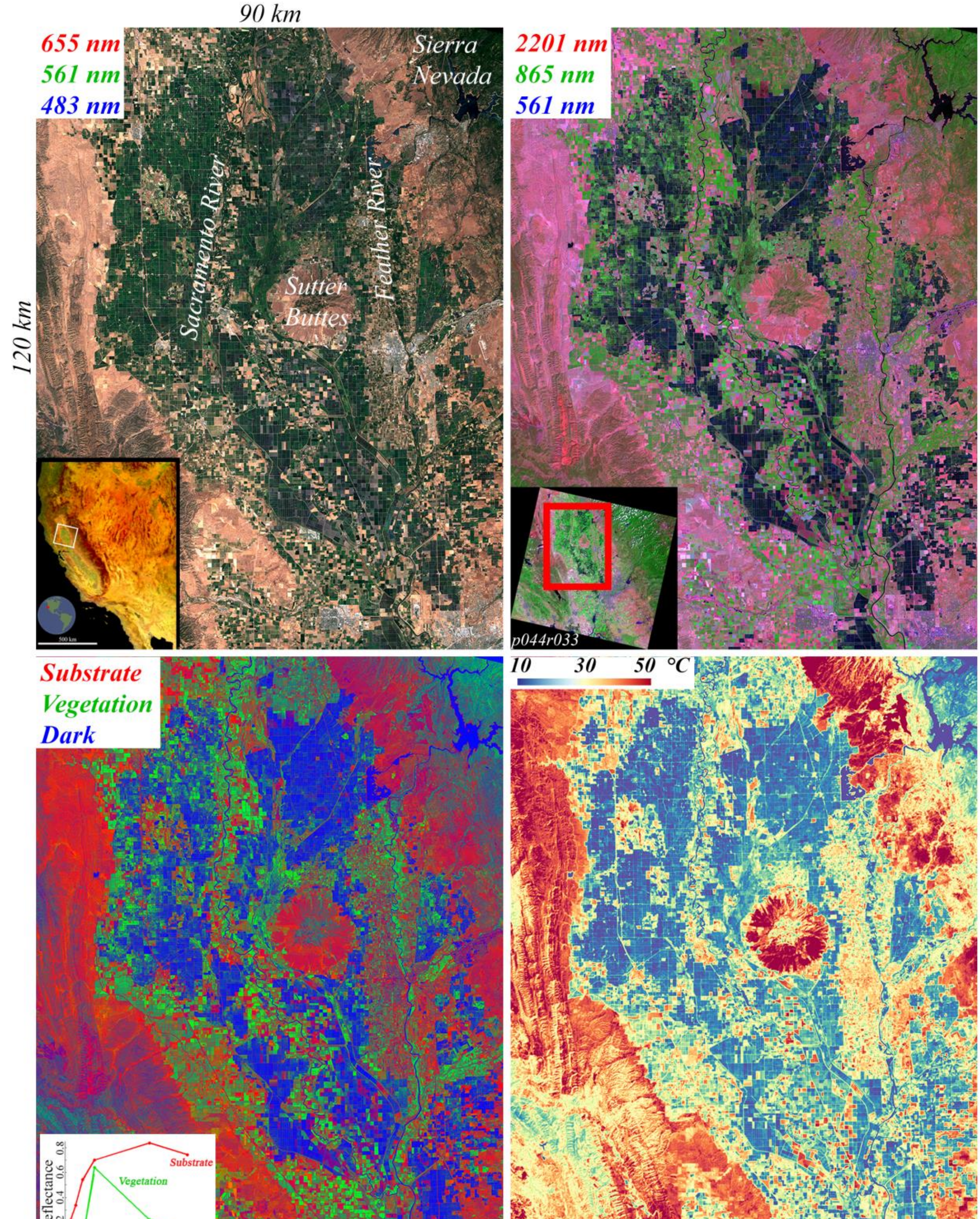

242 Figure 1. The Sacramento Valley. True color (UL), false color (UR), fraction abundance (LL) and thermal (LR) images of a diverse northern CA landscape as imaged by Landsat 8 on June 19, 2013. Green fields are generally distinct from fallow fields and grasslands in the visible, but infrared bands shown in the false color composite allow superior discrimination. At this time of year, nearly all flooded fields are rice and nearly all green, not flooded fields are row crops & orchards. S, V, D subpixel abundances are estimated using a 3 EM spectral mixture model. Visual agreement between the S fraction and T images suggests that regions dominated by S fraction are generally hotter than regions dominated by V or D fractions.

3. Results

3.1. Vegetation Metric Comparison

We begin our analysis with a comparison of vegetation metrics because of their centrality to ET estimation. The left panel of Figure 2 shows bivariate distributions of NDVI, NDVI*, and NDVI^{*2} against SMA-derived vegetation fraction (V) for the 5 most informative June Landsat 8 images in the archive. Images are arranged from top to bottom by increasing Julian Day irrespective of year to illustrate general features of the seasonal phenology of the region.

NDVI shows a nonlinear relationship with V, overestimating at most values and rolling off prominently. The roll-off of the top of the distribution begins below 0.5 and truncates near 0.85, while the roll-off on the bottom appears to be continuous. The consistency of the $NDVI_{max}$ and $NDVI_{min}$ values of 0.85 and 0.15 across all 10 images (including 5 not shown in Fig. 2) justifies the use of a single set of normalization bounds for all images. The residual values of 0.15 in unvegetated areas is largely due to the positive slope at VNIR wavelengths generally present in bare soil spectra. NDVI* better fills the physically meaningful 0 to 1 range expected of fractional vegetation cover, but still has notable overestimation and roll-off effects. NDVI^{*2} is even more linear than NDVI*, but the

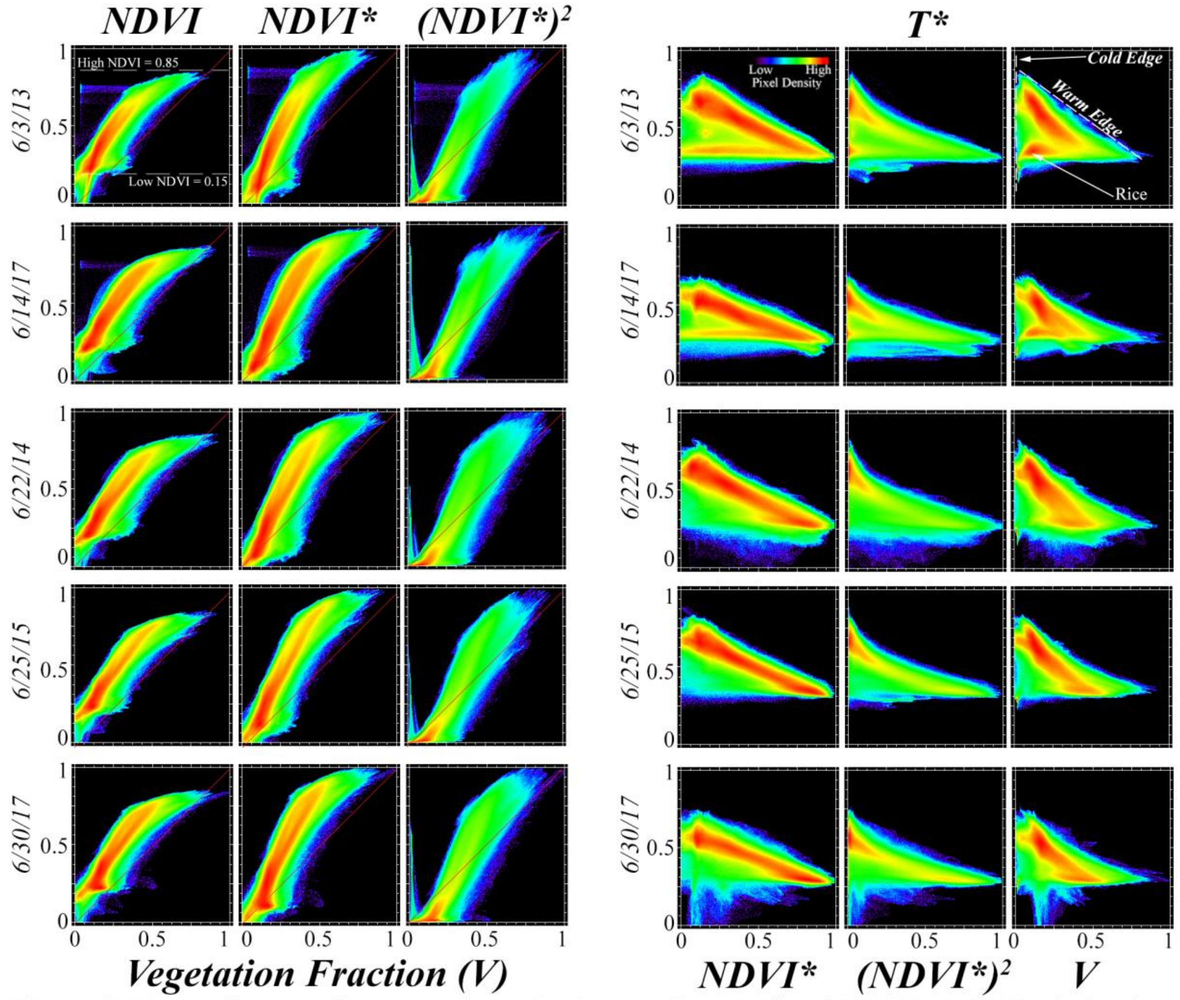

Figure 2. Vegetation metric comparison. L: Raw and normalized NDVI vs SMA-derived vegetation fraction (V). NDVI* is more linear than NDVI, but still shows a bias and saturates near values of 0.85. NDVI^{*2} is more linear yet, but compresses the distribution toward 0. All 3 indices generally overestimate V at intermediate values and roll-off at high values. R: Bivariate distributions of vegetation metrics vs T all form triangular distributions. Dense vegetation is cold and sparse vegetation can have a wide T range. Considerably more structure is evident in the V vs T* distributions than in the index distributions. In early June (top rows), flooded, young rice paddies form a cluster in the V vs T* distributions that is not distinguished by either index, illustrating the inaccuacy of NDVI for sparse vegetation.

distribution is shifted towards smaller values because squaring numbers smaller than 1 reduces their value. The general effect of these rescalings of NDVI appears to be to increase the degree of underestimation at low vegetation fractions, while retaining the overestimation at higher vegetation fractions. Notably, the saturation at high NDVI values, though reduced by the rescalings, still remains. As a result, a wide range of vegetation fractions are placed near $NDVI^{*2}_{max}$. The effects described here are consistent for our study area throughout the entire June Landsat 8 archive.

Bivariate distributions of NDVI*, $NDVI^{*2}$, and V versus T* are shown in the right panel of Figure 2. All three metrics show the expected triangular relationship, but considerably more information is evident using V than either of the spectral indices, visible in the form of internal structure. The overestimation of NDVI* is visible in the pronounced density of points near the upper bound ("warm edge") of the triangle. $NDVI^{*2}$ overcompensates for this effect, compressing the vegetation abundance distribution toward 0 values and leaving the upper portion of the space sparsely populated and concave. In comparison, V retains considerable structure across low, intermediate, and high V values. Physically meaningful clusters are clearly identifiable in the V vs T space which are not distinct in either of the spaces of the spectral indices. One example of this is the paddy rice which plots at low V and T values on the June 3, 2013 image and then progressively migrates toward higher V values in later images as the crop matures and its canopy closes.

Structure (or lack thereof) in the V vs T space maps onto structure in the space of ET parameters. Figure 3a shows this for the ET fraction (EF) using each of the NDVI*, $NDVI^{*2}$, and V vegetation metrics. Every image examined generally forms a triangular shape in EF vs vegetation space, regardless of the vegetation metric. Pixels with high vegetation abundances converge to a single, high EF value, but pixels with low vegetation abundances can have either high (flooded fields or lakes) or low (dry soil or impervious surface) EF values. However, the amount of structure within the pixel envelope varies considerably from metric to metric. The least complex structure is visible in the NDVI* distribution and the most complex structure is visible in the V distribution. The compression of $NDVI^{*2}$ values down toward small values results in a broad base to the triangular cloud, but sparse intermediate estimates. In contrast, the V vs EF plots show considerable pixel density throughout the range of V values, with broad clusters corresponding to physically meaningful land covers. Flooded rice paddies are clearly distinct from green (non-rice) agricultural fields, which are clearly distinct from dry soils. These distinctions in the EF vs vegetation space are much better represented by V than NDVI* or $NDVI^{*2}$.

The Mo vs vegetation space, shown in Figure 3b, can be interpreted similarly. In all cases, a clear triangular structure to the space is again evident. All pixels with high vegetation abundances are associated with low Mo, but pixels with low V values can be associated with high Mo (flooded areas & lakes) or low Mo (dry soil & impervious surface). In some scenes, higher elevation forests in the Sierra Nevada form a distinct cluster in V vs Mo space because they are substantially colder than the rest of the scene. Again, significant differences in internal structure are apparent from metric to metric, with the most complex and informative structure apparent in the V vs Mo space.

3.2. Dark Fraction and Albedo

The D fraction provided by SMA also yields information relevant to ET estimation. Bivariate distributions of D fraction against EF and Mo estimates are shown in the first and third columns of Figure 4. D vs EF spaces show similar overall structure from scene to scene. The pixel envelope is considerably more complex than that of the V vs EF & Mo spaces, reflecting a less direct relationship between D and ET. In early June, rice paddies reside in a consistent cluster at high D and high EF. This cluster is prominently separated from the remainder of the point cloud. As the growing season progresses, D decreases as V increases and the cluster migrates to join the other green (non-rice) agriculture in the upper left corner of the point cloud at high EF values but low D fractions. Dry soil and NPV occupies the lower curvilinear bound of the space with variable D fraction corresponding to illumination, substrate albedo, roughness, and fractional cover of NPV vs soil.

The overall envelope of the D vs Mo distributions (third column of Figure 4) is more triangular than that of the D vs EF distributions. This reflects the propensity for surfaces with high D fractions

309

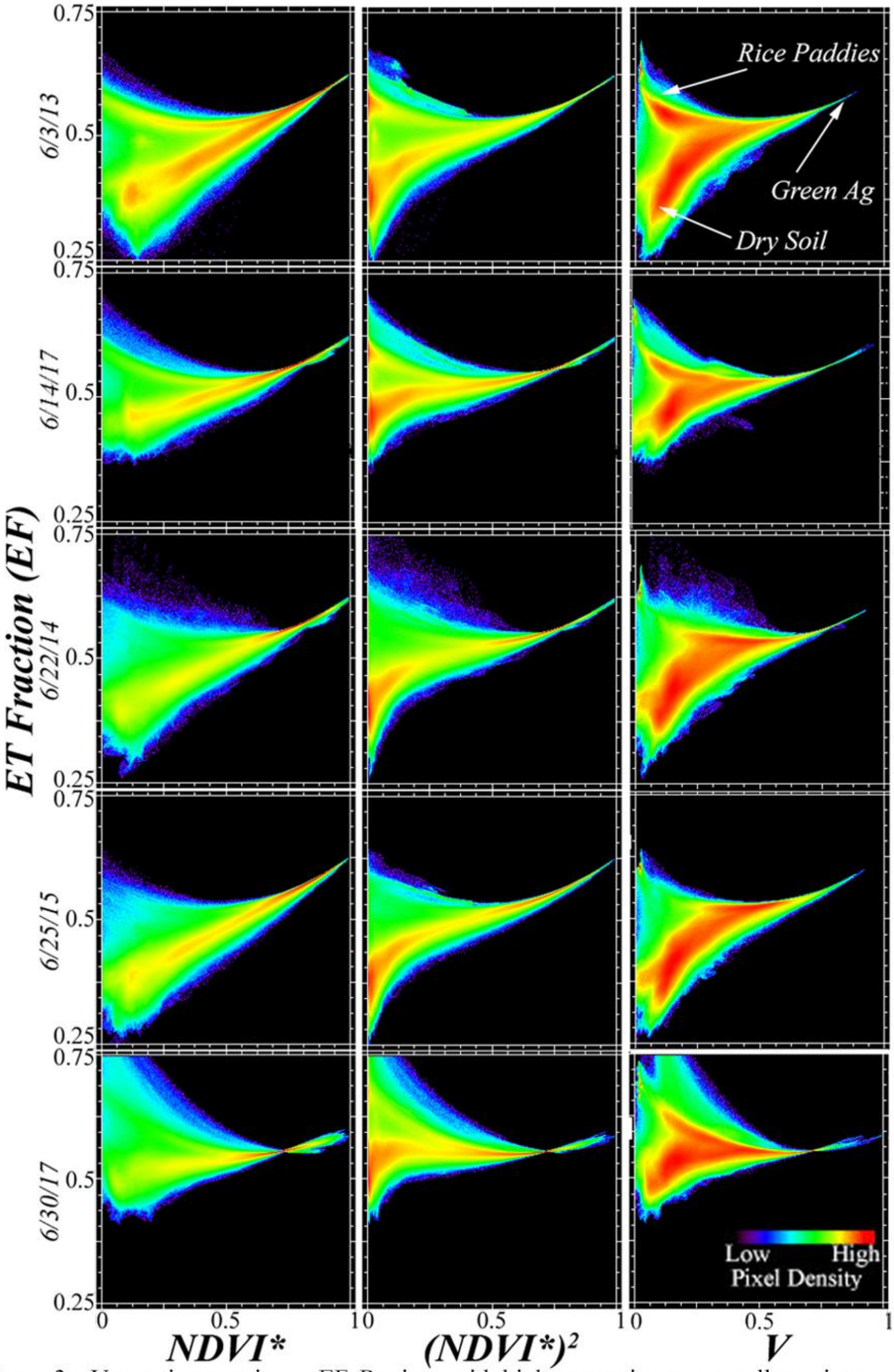

Figure 3a. Vegetation metrics vs EF. Regions with high vegetation cover collapse into a tight range of EF. Regions with low vegetation can have high or low EF. For images earlier in June, the abundance of flooded rice paddies results in a cluster at high EF but low T. This cluster migrates to higher V later in June as the rice canopy fills. Again, NDVI* shows the least structure, NDVI*^{2} is intermediate, and V shows the most structure.

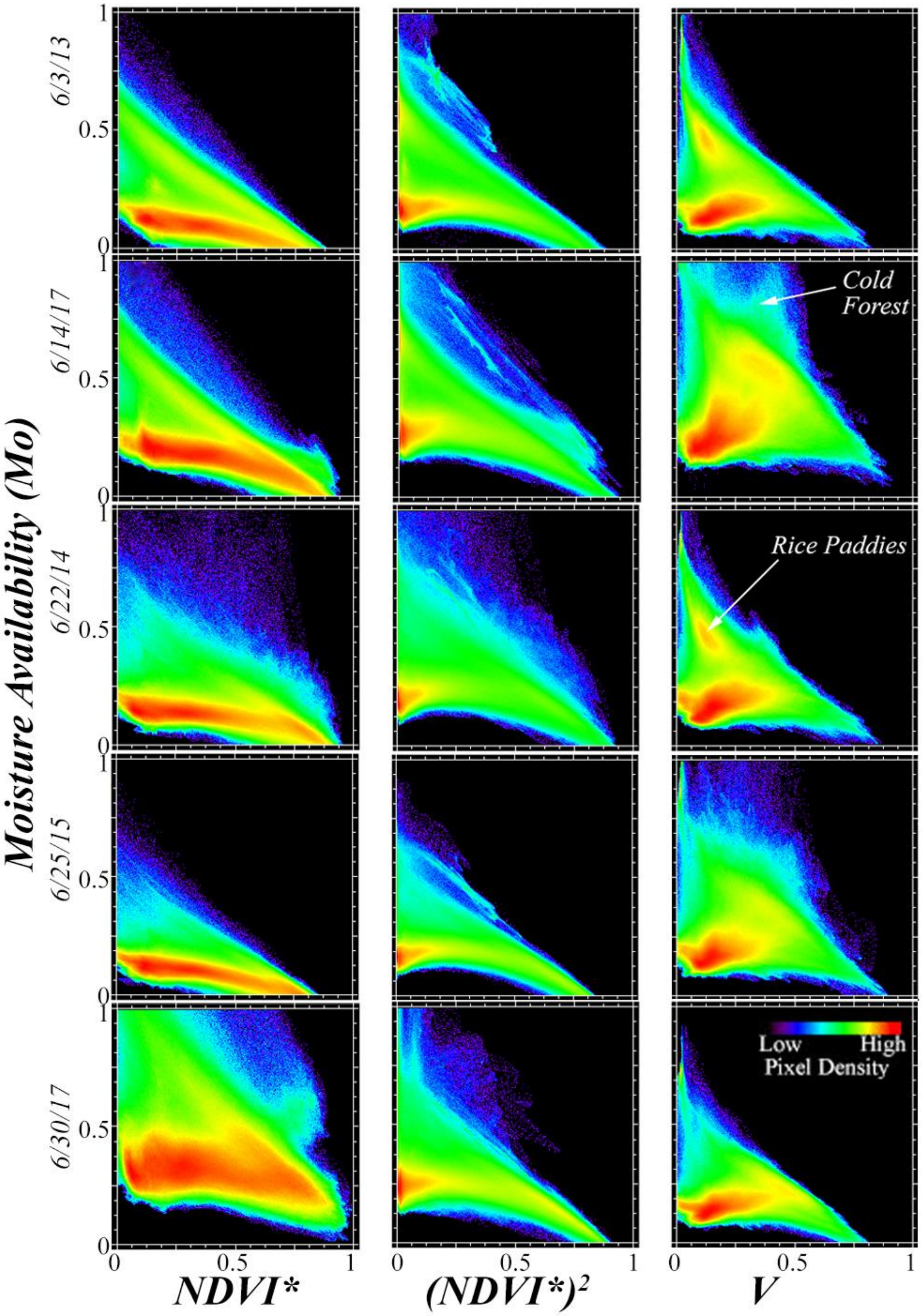

Figure 3b. Vegetation metrics vs Mo. Regions with high vegetation cover converge into a tight range of low Mo. Regions with low cover can have high or low Mo. In some scenes, forests at higher elevation in the NE corner of the image are colder than that rest of the image and so record anomalously high Mo. With V, the rice paddy cluster is again separate in early June, then moves to high V and low Mo values as the canopy fills. This cluster is barely distinguishable, and the structure much less clear, using either spectral index.

311

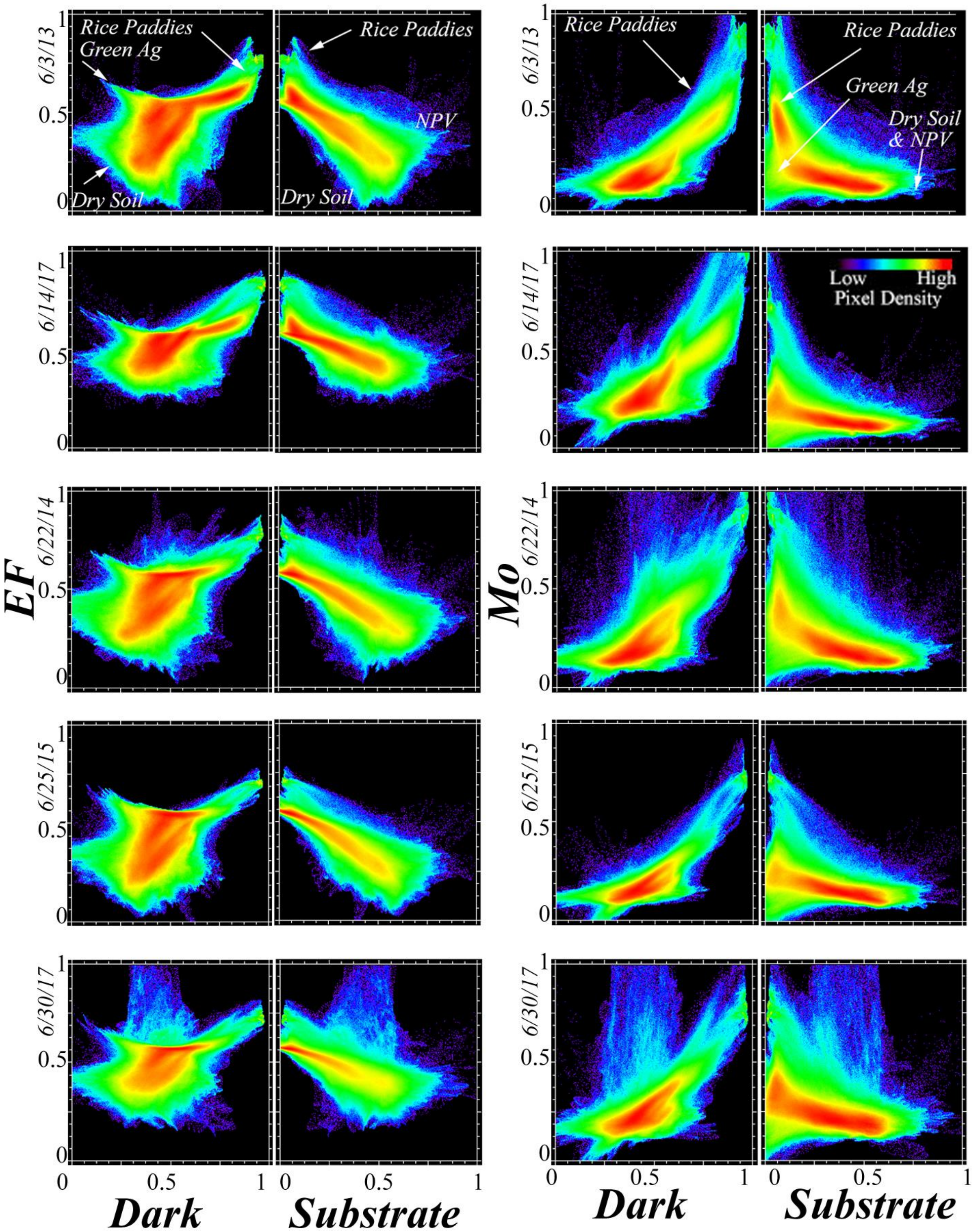

Figure 4. Dark and Substrate Fractions vs EF and Mo. Corresponding α vs EF and Mo spaces are not shown because nearly indistinguishable from the mirror image of the D vs EF and Mo spaces. The rice paddy cluster is present in both D vs EF and D vs Mo spaces, but only weakly in S vs Mo. High EF values are partitioned between green (non-rice) agriculture at low D & low S values and rice paddies at high D and low S values. D vs Mo distributions generally show increasing Mo with increasing D. S vs EF and MO distributions show decreasing EF and MO with increasing S.

to have high moisture content (standing water, saturated soil) or deep shadow. Rice paddies again reside in a consistently isolated cluster in early June, with high values of both D and EF, and migrate toward the remainder of the point cloud as the growing season progresses. Non-rice land cover resides in a more amorphous cluster with intermediate dark fractions and relatively low Mo.

The left and center columns of Figure 5 show the bivariate distribution of D vs T* and α vs T* for each image, respectively. The two distributions have obvious visual similarity and give similar information. Clearly, the D fraction well represents broadband shortwave albedo in these images. Pixels with high D fractions and low α values generally have low T* values, generally corresponding to standing water. Pixels with intermediate D fraction or intermediate α, however, can possess any of the full range of T* values. This is because these pixels can correspond to a wide range of land covers including green crops, forests, dry fields, and impervious surfaces.

3.3. Substrate Fraction, Temperature, and ET

The third complementary piece of information given by the SVD approach is contained in the S fraction. The distributions of S versus EF & Mo are examined in the second and fourth columns of Figure 4. Again, broad similarities in structure are observed between scenes. EF shows a consistent inverse relationship to S, fanning out at higher S values in correspondence to the spectral ambiguity between soil and NPV. In contrast, the relationship between S and Mo is generally triangular and has some visual similarities to the relationship between V and Mo shown in Figure 3b. Pixels with high S values uniformly have low Mo values, accurately representing the low moisture content of bright, dry soils and NPV. However, pixels with low S values can have either high or low Mo values, corresponding to standing water or dense vegetation, respectively. In some scenes, sporadic clouds distort these relationships by yielding spuriously high S values, low T values, and high EF and MO values.

In contrast to the complexity of the V vs T and D vs T distributions, the relationship between S and T is remarkably straightforward in this study area, as shown in the right column of Figure 5. For all 10 June Landsat 8 images in the archive, S fraction shows a simple linear relationship to T. When all the single date spaces are combined into a single multi-date composite space, shown in Figure 6, this relationship is masked because scene-to-scene variations in air temperature and illumination geometry result in shifts in absolute position of the point cloud in T – but not the structure of the point cloud relative to itself. Correlation coefficients for each coincident S vs T image pair, also shown in Figure 6, quantify the strength of this relationship in the 0.7 to 0.9 range, substantially stronger than the (negative) relationship between V and T. Because the relationship between S and T is so strong, the relationship between S and V is similar to the relationship between T and V. The potential implications of this observation could be considerable given that S is quantified using information from the optical bands alone.

4. Discussion

4.1. Application Examples

Figure 7 shows an example of ET estimation using the SVD approach on an August 14, 2016 image in the study area. This image was acquired relatively late in the growing season. In this image, the majority of rice fields have closed canopies and some are beginning to senesce. Orchards are generally in full leaf at this time, and row crops are in various stages of growth. Rice fields are easily identifiable form the SVD image (top) on the basis of their high V fraction, large field size and relatively homogenous internal structure. Orchards generally have lower V fraction and higher S fraction due to bare soil present between rows of trees. Native vegetation in the wildlife refuges and grasslands is generally senescent at this time of year, resulting in low V fractions and high S fractions. Human settlements show considerable complexity, generally resulting in high S and D fractions.

361

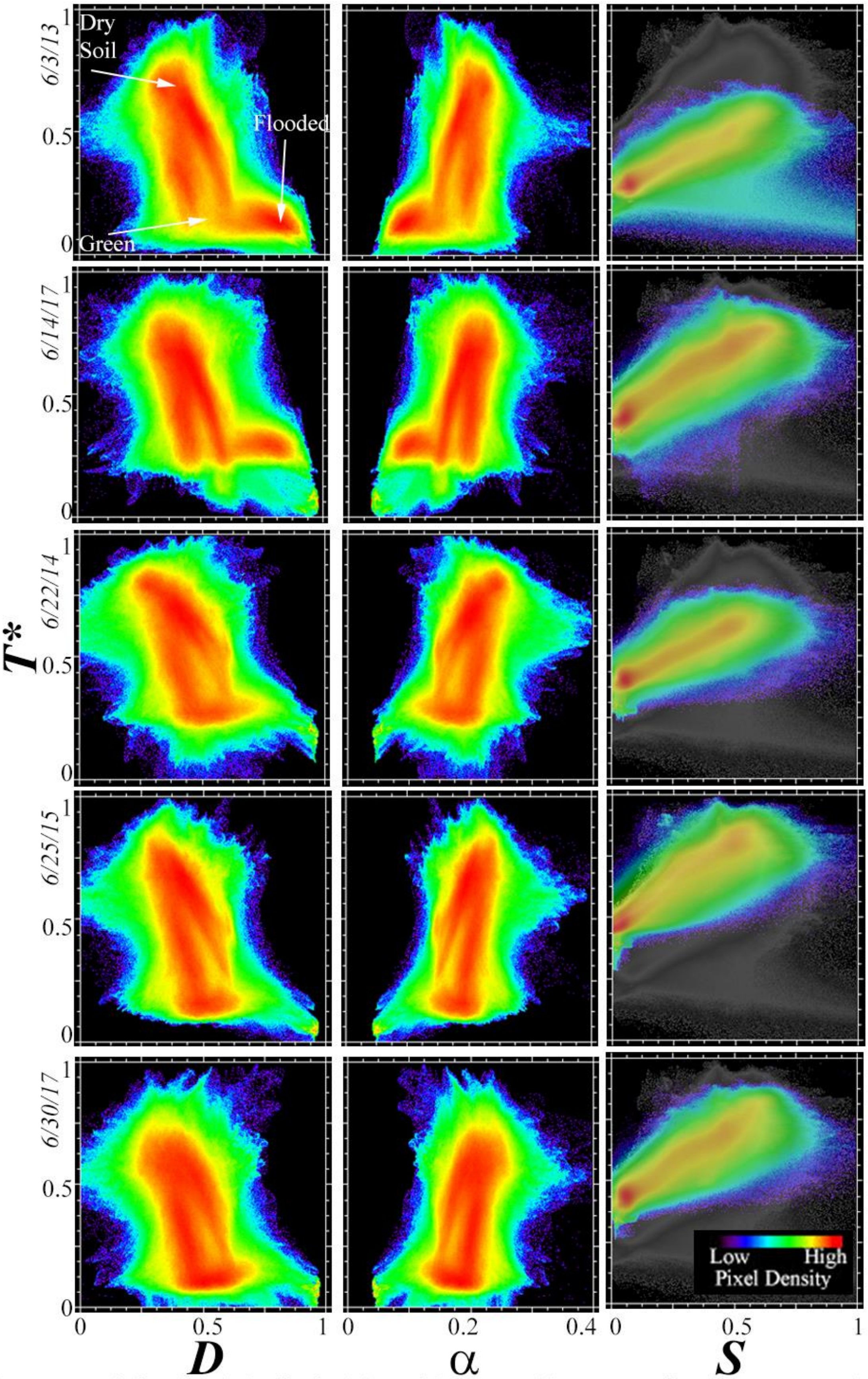

Figure 5. Dark fraction (D), albedo (α), and Substrate (S) vs normalized temperature (T*). The D vs T* relation is similar to the α vs T* relation (with a sign flip). In contrast, the S vs T relation is highly linear. Pixels which are cooler than the main S vs T relation are generally covered with NPV and pixels hotter generally correspond to low albedo soils.

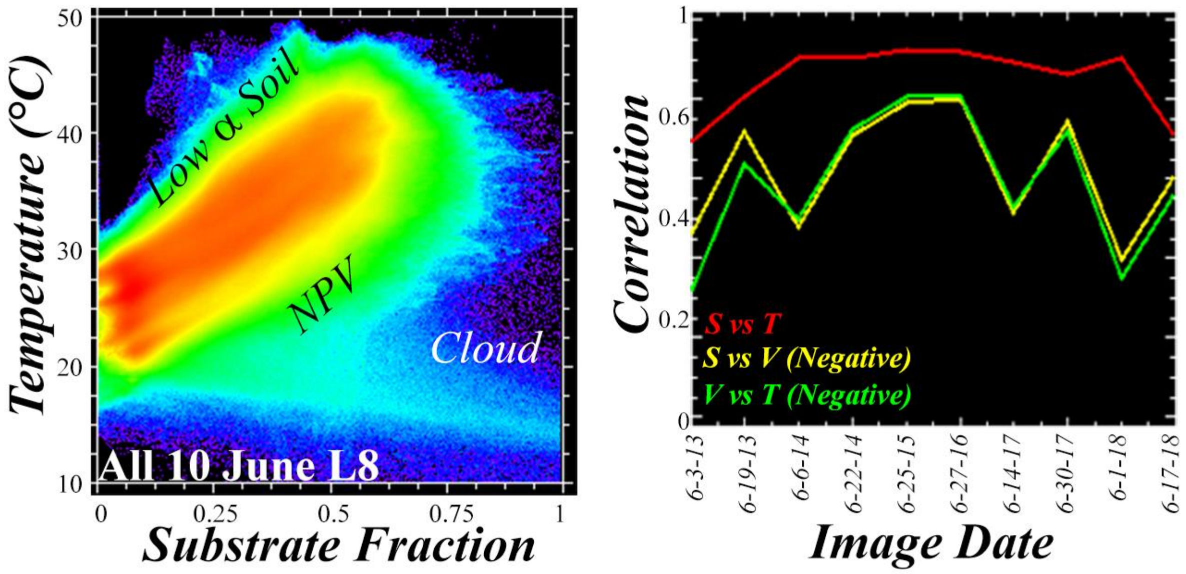

Figure 6. Composite relationship between S and T. Left: A consistent linear relationship between S and T is observed for nearly every June scene in the Landsat 8 archive, but the composite space of all 10 acquisitions is less obviously linear because significant image-to-image variability exists in air temperature. Right: Correlation between coincident S, V and T images for each date. The observed (+) correlation between S and T is stronger in every case than the well-known (-) correlation between V and T. Because the S vs T correlation is so strong, the V vs S and V vs T correlations are very similar.

Variations in V fraction and T images are manifest in the EF and Mo images (center and bottom, respectively). EF shows highest values in the rice fields and lowest values in the dry grasslands and fallow fields, consistent with physical expectations. Wildlife refuges show substantial internal structure due to their complex land cover mosaic of water, native plants, and managed vegetation. Orchards and row crops show intermediate EF values. In contrast, the Mo image reveals different spatial patterns. Considerably more internal structure is evident in the rice growing region in the Mo image than the EF image, consistent with spatial variations in field maturity. Rice in the western portion of this scene was planted earlier than in the east, resulting in more rapid senescence and reduced Mo in the west relative to the east. The spatial structure in the wildlife refuges observed in the EF image is greatly diminished in the Mo image, where the region is characterized by relatively homogenous low Mo values.

Figure 8 presents in greater spatial detail a 24 x 24 km spatial subset indicated by the white box in Figure 7. The image shown in Figure 8 was collected earlier in the growing season, on June 19, 2013. The false color image (A), together with the coincident thermal image (B), allow for broad discrimination between land cover types. The cold, black-to-green large rectilinear fields correspond to flooded paddies with early stage rice growing in them. Warmer, brighter areas along the Sacramento River channel correspond to row crops and orchards growing in sandier soils. The settlement of Willows, CA is present in the northwest corner of the image, with a complex reflectance signature and elevated temperatures relative to the surrounding agricultural landscape. A wildlife preserve is also present in the southwest corner of the image, characterized by a complex reflectance and temperature mosaic. SVD fractions (C) quantify this diversity through amplitude variations of three continuous fields.

NDVI*, NDVI*^{2}, and V are shown in D-F. Relative to V, NDVI* underestimates vegetative cover in the settlement and wildlife preserve areas and overestimates it in some areas of rice agriculture. The overestimation in the rice is even more severe for NDVI*^{2}, although the underestimation in the wildlife refuge and settlement areas appears less severe. These differences in estimates of fractional vegetation cover then map onto estimates of EF (G-I) and Mo (J-L) using each metric. The overall spatial pattern of EF does not have extreme variations from metric to metric, although prominent differences are evident within the region of rice agriculture as well as the settlement. Mo estimates, on the other hand, are wildly variable. While the spatial pattern of Mo estimated using V appears to

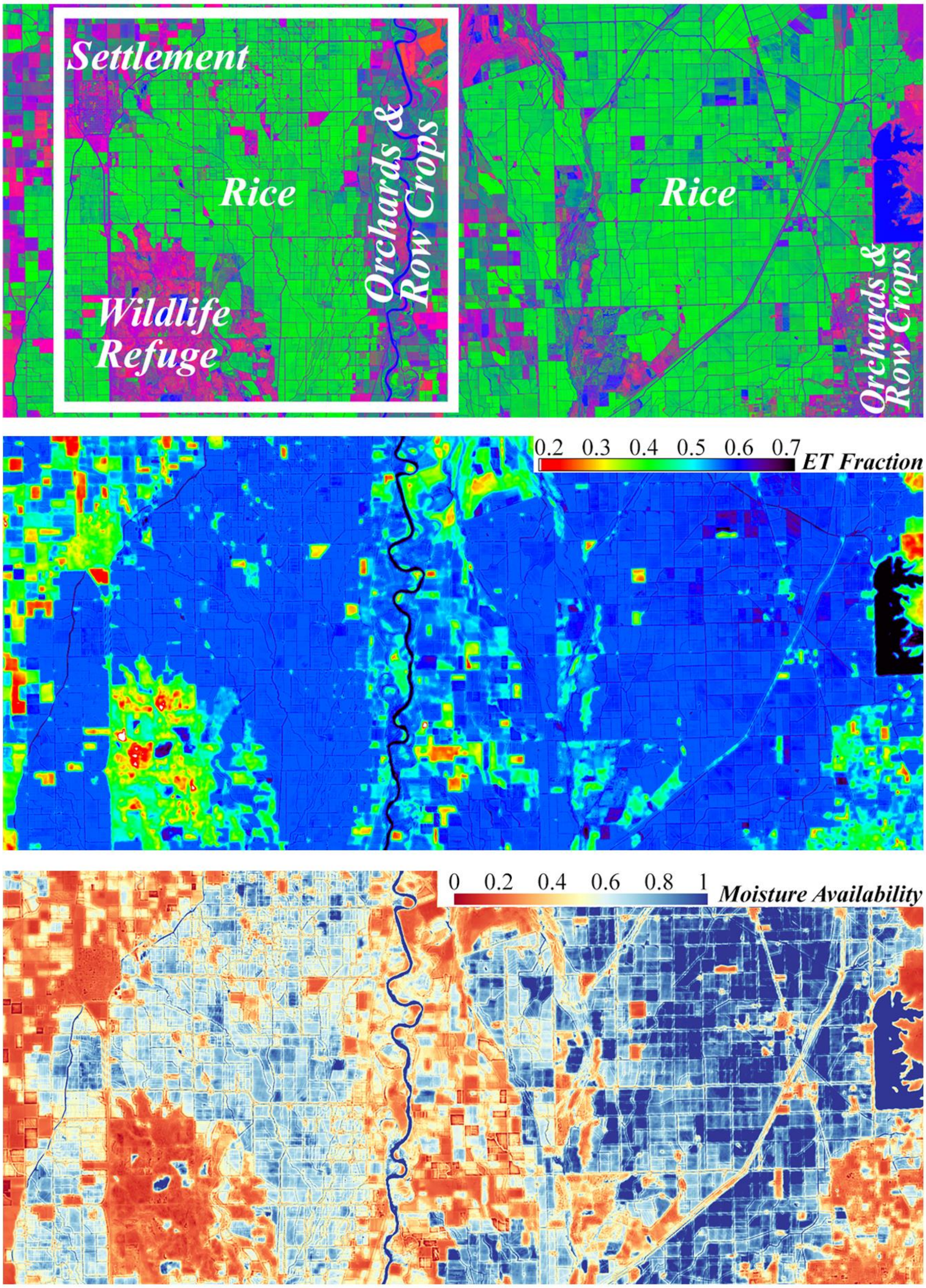

Figure 7. Comparison in map view. SVD fractions, EF & MO for a sample 15 x 50 km region. Flooded paddies have high V and high Mo and EF. The fields in the western half of this August image were planted earlier than the eastern half and have started to senesce, resulting in lower Mo. Orchards have lower EF and Mo. The wildlife refuge is complex, with both high and low EF and Mo. Landsat 8 resolves heterogeneity both within individual fields as well as across the valley. The white box shows the spatial subset used for Figure 8.

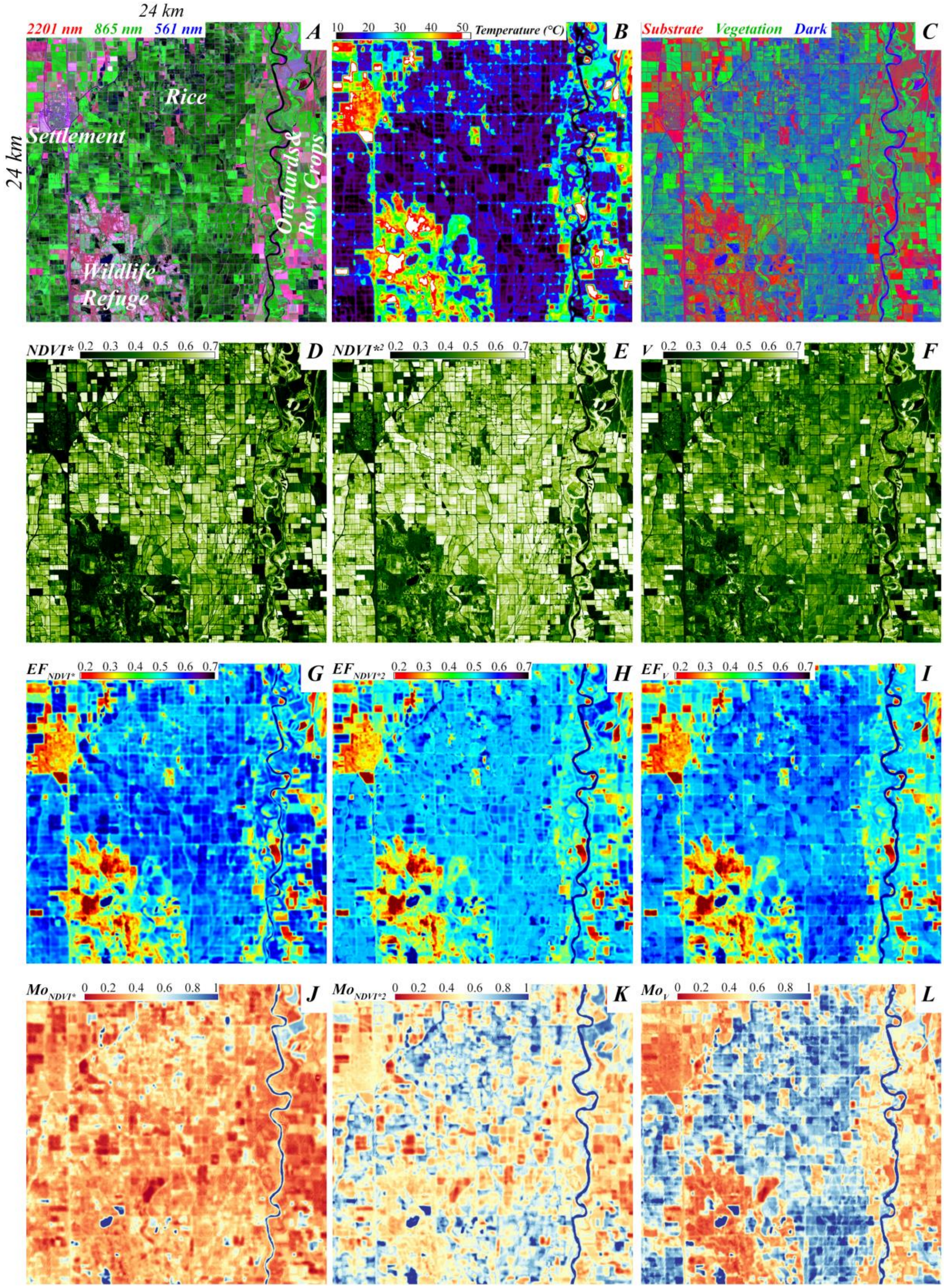

Figure 8. Example ET comparison. Landsat 8 collected coincident optical (A) and thermal (B) imagery on June 19, 2013. SVD fraction image (C) reveals substantial spatial heterogeneity in agricultural and preserved lands. NDVI* (D) and NDVI*[2] (E) images show substantial differences from each other and from V (G). EF estimates using the 3 vegetation metrics (G-I) show similar overall patterns, but notable differences within agricultural areas. Differences in Mo (J-L) estimates are even more profound.

393

match the physical properties of the landscape mosaic, Mo estimated using the spectral indices does not appear to capture even the prominent differences between the dry wildlife refuge and settlement and the flooded rice paddies. The differences in EF and Mo estimates illustrate the potential sensitivity of ET estimation to vegetation metric and the opportunity for improvement in current estimates using the SVD approach.

4.2. ET Partitioning

A recent global analysis has shown the partitioning of ET into its primary subcomponents of transpiration (leaf water to air), soil evaporation (soil moisture to air), and interception evaporation (plant surface water to air) to vary widely between common ET models [63]. Further work (published in this Special Issue) shows NDVI to be the primary sensitivity of the Priestley-Taylor Jet Propulsion Laboratory (PT-JPL) ET model, with substantial nonlinearity [64]. As mentioned in [64], nonlinearities in model formulation may explain this result. In addition, we suggest that another factor potentially contributing to this sensitivity could be the generally nonlinear relationship between NDVI, the model input parameter, and fractional vegetation abundance, the physical quantity it is intended to represent. This hypothesis could be easily investigated through trials with simple replacement of NDVI with SMA-estimated V. If the hypothesis is supported and improvement is seen, replacement of NDVI with V could offer a straightforward pathway towards ET model improvement with a minimum of effort.

This opportunity is not unique to the PT-JPL model. Many ET model formulations assume a simple relationship between a biogeophysical landscape quantity such as fractional vegetation abundance and a spectral index. A robust body of previous work (partially reviewed in the Background section above) has shown SMA to outperform spectral indices in a wide range of environments and spatial resolutions, especially in the case of broadband multispectral imagery. SMA also has the advantage of being grounded in a straightforward physical basis and accounts for the effects of soil reflectance, moisture content and shadow explicitly. In general, it is reasonable to expect the relationship between the true subpixel areal abundance of land cover and the estimate given by SMA to be more accurate, and scale more linearly, than the estimate given by a spectral index. Given the ease with which SMA can be implemented into multispectral image processing workflows, and the current prevalence of spectral vegetation indices in ET models, this presents a substantial opportunity for the improvement of remote sensing-based estimation of ET.

4.3. Thermal EM Selection

ET estimation methods that rely on the regional V vs T relation are generally sensitive to the selection of hot and cold thermal endmembers [65–67]. As noted by [68], the hot & cold EMs fundamentally set SVAT model boundary conditions and thus constrain the distribution of possible ET outcomes. Because of this, ET models rooted in the V vs T relation can fundamentally only be as accurate and as consistent as the thermal EMs used in their formulation.

The SVD approach provides users with additional information about potential thermal EMs by providing two additional quantities relating to the land cover of the pixel. This information could be especially useful when considering the choice of hot EM, a particularly important and sensitive point, as noted by [66]. The two parameters of spectral vegetation index and brightness temperature alone are generally insufficient to reliably distinguish between such widely variable materials as asphalt (or other low albedo anthropogenic surfaces), dry NPV (standing or cut crop litter, senesced grass), dry low albedo soil, and dry high albedo soil. However, by adding S and D fraction information, these materials can be readily distinguished using their position in a 4-dimensional parameter space. This enhanced ability to discriminate between potential hot EM materials could support attempts to improve the consistency and accuracy of thermal EM selection.

4.4. Clustering in Fraction vs ET Space

The structure of the SVD fraction vs ET spaces is a key component of this analysis. Both broad consistencies and illuminating differences are present between images in each space. Clustering in this space, indicative of landscape subsets with similar land cover and ET combinations, can be useful for mapping distinct land cover types. For example, the flooded rice paddies common in the study area are shown in Figures 3-5 as occupying a distinct position in each of the S, V, and D vs T, EF and Mo spaces. The position of these paddies relative to the other points in the space migrates throughout the growing season, resulting in a set of trajectories characteristic of rice paddies which are distinct from those of other types of crops, grasslands, or non-agricultural vegetation.

Clustering in the feature space is also the foundation for discrete image classification. By contributing an additional (although not independent) set of basis vectors for the multispectral feature space, ET estimates offer an additional opportunity to help statistical classification algorithms resolve distinctions between the spectral-thermal properties of different land covers. Especially when approached from a multitemporal framework [69], this information could potentially be used to improve image classification algorithms used for the mapping and monitoring of both human-modified and wilderness landscapes.

4.5. The SVD Approach as a Unifying Framework

The relationships shown in Figures 2-6, and the examples shown in Figures 7 and 8, illustrate the value of SMA with globally standardized SVD EMs as a unifying framework for two complementary approaches to ET investigation: the V vs T relationship and the α vs T relationship. Figures 2 and 3 illustrate the ET-specific advantages of using V over currently used metrics such as NDVI* and NDVI*^{2} on the basis of the enhanced clustering and structure in the V vs T, EF, and MO distributions. These advantages, in addition to previously demonstrated scaling and background suppression properties, advocate for the use of SMA-derived V fraction in ET studies.

In addition to V, the SVD approach simultaneously retrieves information on the other two factors influencing ET; fractional soil exposure and soil moisture. The left and center columns of Figure 5 show this information from the D fraction to be highly similar to (inverted) broadband shortwave albedo. The right column of Figure 5 and Figure 6 show that S fractions are strongly linearly related to T, at least in June imagery in this study area. While this relationship does have a strong physical basis, more investigation is warranted to confirm its generality in other environments and seasons. However, the agricultural and soil complexity in the Sacramento Valley suggest that the relationship may hold in other agricultural environments. By synthesizing the contributions of both vegetation abundance and albedo, the SVD approach presents a unified framework for considering two of the main branches of the ET literature.

The focus of this analysis on a single study area may beg the question of generality of results. While the persistence of the feature space structure over several years is encouraging, it does not guarantee that the method will perform as well in other environments. However, the global analysis of [70] did find a remarkable similarity of structure in the SVD fraction vs T spaces of 24 diverse urban-rural gradients spanning a very wide range of environments and land cover types. While the abundance of impervious surface in those environments complicates interpretation in terms of ET, a simple comparison of the SVD vs T spaces from [70] with those in this analysis shows obvious similarities. The strong linearity of the S vs T space observed in the California study area is not a general feature in the global analysis, although it does appear in some examples containing abundant agriculture (e.g. Calgary, Essen & Cairo). An intercomparison of a diverse sample of agricultural areas worldwide is the focus of a separate study.

Finally, the clustering that is apparent in the S, V & D fractions versus T*, Mo and EF spaces suggests that these spaces could provide the basis for either continuous or discrete classifications of crop types and growth stages for agricultural monitoring. This approach could be particularly effective when combined with spatiotemporal analysis of phenological information derived from multitemporal observations, as proposed by [69]. In addition, once planned global hyperspectral missions become a reality, the SVD framework could be integrated with targeted narrowband approaches such as that of [71].

5. Conclusions

The primary purpose of this study is to demonstrate the potential for spectral mixture analysis (SMA) based on globally standardized Substrate, Vegetation, and Dark (SVD) endmembers (EMs) to provide a comprehensive, integrated framework for ET estimation. The SVD approach yields complementary continuous fields estimating the subpixel fractional abundance of each EM. V fraction is an accurate, linearly scalable metric for vegetation abundance. D fraction provides information which is very similar to (inverse) albedo. S fraction provides information about the soil and NPV substrate background. Using the Triangle method as an example model, the results of this analysis show substantially enhanced structure in both ET fraction (EF) and moisture availability (Mo) estimates based on V fraction than the popularly used NDVI* or $NDVI^{*2}$. Using the coefficients of [62], we show the D vs T relationship to be very similar to broadband shortwave albedo (α) vs T. Finally, we show S to have a consistent, simple linear relationship with T, at least in this study area during peak growing and insolation season. SMA allows globally standardized S, V and D fractions to be estimated simultaneously, with high accuracy and at trivial computational cost. The implications of such a unified framework for standardization and accuracy improvement of ET models could be considerable.

Funding: Work done by DS was conducted with Government support under FA9550-11-C-0028 and awarded by the Department of Defense, Air Force Office of Scientific Research, National Defense Science and Engineering Graduate (NDSEG) Fellowship, 32 CFR 168a. CS gratefully acknowledges the support of the NASA Multi-Source Land Imaging Program (grant 14-LCLUC003).

Acknowledgments: DS thanks Carl and Victor Akers for inspiration and insight.

Conflicts of Interest: The authors declare no conflict of interest.

References

1. Carlson, T.N.; Gillies, R.; Perry, E. A method to make use of thermal infrared temperature and NDVI measurements to infer surface soil water content and fractional vegetation cover. *Remote Sens. Rev.* **1994**, *9*, 161–173, doi:10.1080/02757259409532220.
2. Price, J.C. Using spatial context in satellite data to infer regional scale evapotranspiration. *IEEE Trans. Geosci. Remote Sens.* **1990**, *28*, 940–948.
3. Miralles, D.G.; De Jeu, R.A.M.; Gash, J.H.C.; Holmes, T.R.H.; Dolman, A.J. Magnitude and variability of land evaporation and its components at the global scale. **2011**.
4. Zhang, Y.; Peña-Arancibia, J.L.; McVicar, T.R.; Chiew, F.H.S.; Vaze, J.; Liu, C.; Lu, X.; Zheng, H.; Wang, Y.; Liu, Y.Y.; Miralles, D.G.; Pan, M. Multi-decadal trends in global terrestrial evapotranspiration and its components. *Sci. Rep.* **2016**, *6*, 19124.
5. Miralles, D.G.; van den Berg, M.J.; Gash, J.H.; Parinussa, R.M.; de Jeu, R.A.M.; Beck, H.E.; Holmes, T.R.H.; Jiménez, C.; Verhoest, N.E.C.; Dorigo, W.A.; Teuling, A.J.; Johannes Dolman, A. El Niño–La Niña cycle and recent trends in continental evaporation. *Nat. Clim. Chang.* **2013**, *4*, 122.
6. Miralles, D.G.; Van Den Berg, M.J.; Teuling, A.J.; De Jeu, R.A.M. Soil moisture-temperature coupling: A multiscale observational analysis. *Geophys. Res. Lett.* **2012**, *39*.
7. Jackson, R.D.; Reginato, R.J.; Idso, S.B. Wheat canopy temperature: a practical tool for evaluating water requirements. *Water Resour. Res.* **1977**, *13*, 651–656.
8. Jackson, R.D.; Idso, S.B.; Reginato, R.J.; Pinter Jr, P.J. Canopy temperature as a crop water stress indicator. *Water Resour. Res.* **1981**, *17*, 1133–1138.
9. Idso, S.B.; Jackson, R.D.; Reginato, R.J. Remote-Sensing of Crop Yields. *Science (80-.).* **1977**, *196*, 19 LP-25.
10. Anderson, M.; Allen, R.G.; Morse, A.; Kustas, W.P. Use of Landsat thermal imagery in monitoring evapotranspiration and managing water resources. *Remote Sens. Environ.* **2012**, *122*.
11. Fisher, J.B.; Melton, F.; Middleton, E.; Hain, C.; Anderson, M.; Allen, R.; McCabe, M.F.; Hook, S.; Baldocchi, D.; Townsend, P.A.; Kilic, A.; Tu, K.; Miralles, D.D.; Perret, J.; Lagouarde, J.; Waliser, D.; Purdy, A.J.; French, A.; Schimel, D.; Famiglietti, J.S.; Stephens, G.; Wood, E.F. The future of evapotranspiration: Global requirements for ecosystem functioning, carbon and climate feedbacks, agricultural management, and water resources. *Water Resour. Res.* **2017**, *53*, 2618–2626, doi:10.1002/2016WR020175@10.1002/(ISSN)1944-9208.COMHES1.
12. Fisher, J.B.; Whittaker, R.J.; Malhi, Y. ET come home: potential evapotranspiration in geographical ecology. *Glob. Ecol. Biogeogr.* **2011**, *20*, 1–18, doi:10.1111/j.1466-8238.2010.00578.x.
13. Allen, R.G.; Tasumi, M.; Trezza, R. Satellite-based energy balance for mapping evapotranspiration with internalized calibration (METRIC) Model. *J. Irrig. Drain. Eng.* **2007**, *133*, 380–394.
14. Bastiaanssen, W.; Menenti, M.; Feddes, R.A.; Holtslag, A.A.M. A remote sensing surface energy balance algorithm for land (SEBAL). 1. Formulation. *J. Hydrol.* **1998**, *212–213*, 198–212, doi:10.1016/S0022-1694(98)00253-4.
15. Carlson, T.N.; Boland, F.E. Analysis of urban-rural canopy using a surface heat flux/temperature model. *J. Appl. Meteorol.* **1978**, *17*, 998–1013.
16. Moran, M.S.; Clarke, T.R.; Inoue, Y.; Vidal, A. Estimating crop water deficit using the relation between surface-air temperature and spectral vegetation index. *Remote Sens. Environ.* **1994**, *49*, 246–263.
17. Menenti, M.; Bastiaanssen, W.; Van Eick, D.; El Karim, M.A.A. Linear relationships between surface reflectance and temperature and their application to map actual evaporation of groundwater. *Adv. Sp. Res.* **1989**, *9*, 165–176.

18. Ångström, A. The Albedo of Various Surfaces of Ground. *Geogr. Ann.* **1925**, *7*, 323–342 CR–Copyright © 1925 Swedish Societ, doi:10.2307/519495.
19. Idso, S.B.; Jackson, R.D.; Reginato, R.J.; Kimball, B.A.; Nakayama, F.S. The dependence of bare soil albedo on soil water content. *J. Appl. Meteorol.* **1975**, *14*, 109–113.
20. Matthias, A.D.; Fimbres, A.; Sano, E.E.; Post, D.F.; Accioly, L.; Batchily, A.K.; Ferreira, L.G. Surface roughness effects on soil albedo. *Soil Sci. Soc. Am. J.* **2000**, *64*, 1035–1041.
21. Roerink, G.J.; Su, Z.; Menenti, M. S-SEBI: A simple remote sensing algorithm to estimate the surface energy balance. *Phys. Chem. Earth, Part B Hydrol. Ocean. Atmos.* **2000**, *25*, 147–157.
22. Merlin, O.; Chirouze, J.; Olioso, A.; Jarlan, L.; Chehbouni, G.; Boulet, G. An image-based four-source surface energy balance model to estimate crop evapotranspiration from solar reflectance/thermal emission data (SEB-4S). *Agric. For. Meteorol.* **2014**, *184*, 188–203.
23. Jiang, L.; Islam, S. A methodology for estimation of surface evapotranspiration over large areas using remote sensing observations. *Geophys. Res. Lett.* **1999**, *26*, 2773–2776.
24. Kustas, W.P.; Norman, J.M.; Anderson, M.C.; French, A.N. Estimating subpixel surface temperatures and energy fluxes from the vegetation index-radiometric temperature relationship. *Remote Sens. Environ.* **2003**, *85*, 429–440.
25. Elmore, A.J.; Mustard, J.F.; Manning, S.J.; Lobell, D.B. Quantifying vegetation change in semiarid environments: precision and accuracy of spectral mixture analysis and the normalized difference vegetation index. *Remote Sens. Environ.* **2000**, *73*, 87–102.
26. Small, C. Estimation of urban vegetation abundance by spectral mixture analysis. *Int. J. Remote Sens.* **2001**, *22*, 1305–1334.
27. Smith, M.O.; Ustin, S.L.; Adams, J.B.; Gillespie, A.R. Vegetation in deserts: I. A regional measure of abundance from multispectral images. *Remote Sens. Environ.* **1990**, *31*, 1–26.
28. Small, C.; Milesi, C. Multi-scale standardized spectral mixture models. *Remote Sens. Environ.* **2013**, *136*, 442–454.
29. Choudhury, B.J.; Ahmed, N.U.; Idso, S.B.; Reginato, R.J.; Daughtry, C.S. Relations between evaporation coefficients and vegetation indices studied by model simulations. *Remote Sens. Environ.* **1994**, *50*, 1–17.
30. Carlson, T.N. An Overview of the “Triangle Method” for Estimating Surface Evapotranspiration and Soil Moisture from Satellite Imagery. *Sensors* **2007**, *7*, 1612–1629, doi:10.3390/s7081612.
31. Carlson, T.N.; Ripley, D.A. On the relation between NDVI, fractional vegetation cover, and leaf area index. *Remote Sens. Environ.* **1997**, *62*, 241–252.
32. Sun, H. A Two-Source Model for Estimating Evaporative Fraction (TMEF) Coupling Priestley-Taylor Formula and Two-Stage Trapezoid. *Remote Sens.* 2016, *8*.
33. Adams, J.B.; Smith, M.O.; Johnson, P.E. Spectral mixture modeling: A new analysis of rock and soil types at the Viking Lander 1 site. *J. Geophys. Res. Solid Earth* **1986**, *91*, 8098–8112.
34. Gillespie, A.R.; Smith, M.O.; Adams, J.B.; Willis, S.C.; Fischer, A.F.; Sabol, D.E. Interpretation of residual images: spectral mixture analysis of AVIRIS images, Owens Valley, California. In *Annual JPL Airborne Visible/Infrared Imaging Spectrometer (AVIRIS) Workshop*; 1990; Vol. 2, pp. 54–90.
35. Smith, M.O.; Johnson, P.E.; Adams, J.B. Quantitative determination of mineral types and abundances from reflectance spectra using principal components analysis. *J. Geophys. Res. Solid Earth* **1985**, *90*, C797–C804.
36. Baldocchi, D.; Krebs, T.; Leclerc, M.Y. “Wet/dry Daisyworld”: a conceptual tool for quantifying the spatial scaling of heterogeneous landscapes and its impact on the subgrid variability of energy fluxes. *Tellus B Chem. Phys. Meteorol.* **2005**, *57*, 175–188, doi:10.3402/tellusb.v57i3.16538.

37. Brunsell, N.; Gillies, R. Length Scale Analysis of Surface Energy Fluxes Derived from Remote Sensing. *J. Hydrometeorol.* **2003**, *4*, 1212–1219, doi:10.1175/1525-7541(2003)004<1212:LSAOSE>2.0.CO;2.
38. McCabe, M.F.; Wood, E.F. Scale influences on the remote estimation of evapotranspiration using multiple satellite sensors. *Remote Sens. Environ.* **2006**, *105*, 271–285, doi:10.1016/J.RSE.2006.07.006.
39. Brunsell, N.; Anderson, M. Characterizing the multi–scale spatial structure of remotely sensed evapotranspiration with information theory. *Biogeosciences* **2011**, *8*, 2269–2280, doi:10.5194/bg-8-2269-2011.
40. Ershadi, A.; McCabe, M.F.; Evans, J.P.; Walker, J.P. Effects of spatial aggregation on the multi-scale estimation of evapotranspiration. *Remote Sens. Environ.* **2013**, *131*, 51–62, doi:10.1016/J.RSE.2012.12.007.
41. Sharma, V.; Kilic, A.; Irmak, S. Impact of scale/resolution on evapotranspiration from Landsat and MODIS images. *Water Resour. Res.* **2016**, *52*, 1800–1819, doi:10.1002/2015WR017772.
42. Small, C. The Landsat ETM+ spectral mixing space. *Remote Sens. Environ.* **2004**, *93*, 1–17, doi:http://dx.doi.org/10.1016/j.rse.2004.06.007.
43. Sousa, D.; Small, C. Global cross-calibration of Landsat spectral mixture models. *Remote Sens. Environ.* **2017**, *192*, doi:10.1016/j.rse.2017.01.033.
44. Anderson, M.; Norman, J.; Mecikalski, J.R.; Torn, R.D.; Kustas, W.P.; Basara, J.B. A multiscale remote sensing model for disaggregating regional fluxes to micrometeorological scales. *J. Hydrometeorol.* **2004**, *5*, 343–363.
45. Anderson, M.; Kustas, W.; Norman, J.; Hain, C.; Mecikalski, J.; Schultz, L.; GonzÃ¡lez-Dugo, M.; Cammalleri, C.; D'Urso, G.; Pimstein, A. Mapping daily evapotranspiration at field to continental scales using geostationary and polar orbiting satellite imagery. *Hydrol. Earth Syst. Sci.* **2011**, *15*, 223–239.
46. Anderson, M.C.; Norman, J.M.; Diak, G.R.; Kustas, W.P.; Mecikalski, J.R. A two-source time-integrated model for estimating surface fluxes using thermal infrared remote sensing. *Remote Sens. Environ.* **1997**, *60*, 195–216.
47. Yang, J.; Wang, Y. Estimating evapotranspiration fraction by modeling two-dimensional space of NDVI/albedo and day–night land surface temperature difference: A comparative study. *Adv. Water Resour.* **2011**, *34*, 512–518, doi:https://doi.org/10.1016/j.advwatres.2011.01.006.
48. Galleguillos, M.; Jacob, F.; Prévot, L.; French, A.; Lagacherie, P. Comparison of two temperature differencing methods to estimate daily evapotranspiration over a Mediterranean vineyard watershed from ASTER data. *Remote Sens. Environ.* **2011**, *115*, 1326–1340.
49. Petropoulos, G.; Carlson, T.; Wooster, M.; Islam, S. A review of Ts/VI remote sensing based methods for the retrieval of land surface energy fluxes and soil surface moisture. *Prog. Phys. Geogr.* **2009**, *33*, 224–250.
50. Carter, C.; Liang, S. Comprehensive evaluation of empirical algorithms for estimating land surface evapotranspiration. *Agric. For. Meteorol.* **2018**, *256–257*, 334–345, doi:10.1016/J.AGRFORMET.2018.03.027.
51. Kalma, J.D.; McVicar, T.R.; McCabe, M.F. Estimating land surface evaporation: A review of methods using remotely sensed surface temperature data. *Surv. Geophys.* **2008**, *29*, 421–469.
52. Johnson, P.E.; Smith, M.O.; Taylor-George, S.; Adams, J.B. A semiempirical method for analysis of the reflectance spectra of binary mineral mixtures. *J. Geophys. Res. Solid Earth* **1983**, *88*, 3557–3561.
53. Singer, R.B. Near-infrared spectral reflectance of mineral mixtures: Systematic combinations of pyroxenes, olivine, and iron oxides. *J. Geophys. Res. Solid Earth* **1981**, *86*, 7967–7982.
54. Singer, R.B.; McCord, T.B. Mars-large scale mixing of bright and dark surface materials and implications for analysis of spectral reflectance. In *Lunar and Planetary Science Conference Proceedings*; 1979; pp. 1835–1848.

55. Kauth, R.J.; Thomas, G.S. The Tasseled Cap - a graphic description of the spectral-temporal development of agricultural crops as seen by Landsat. In *Proceedings of the Symposium on Machine Processing of Remotely Sensed Data*; Purdue University: West Lafayette, Indiana, 1976; p. 4B41-4B51.
56. Small, C. Multisource imaging of urban growth and infrastructure using Landsat, Sentinel and SRTM. In *NASA Landsat-Sentinel Science Team Meeting*; Rockville, MD, 2018.
57. Sousa, D.; Small, C. Multisensor analysis of spectral dimensionality and soil diversity in the great central valley of California. *Sensors (Switzerland)* **2018**, *18*, doi:10.3390/s18020583.
58. USGS *Landsat 8 Data Users Handbook, Version 2.0*; Sioux Falls, SD, 2016;
59. Gerace, A.; Montanaro, M. Derivation and validation of the stray light correction algorithm for the thermal infrared sensor onboard Landsat 8. *Remote Sens. Environ.* **2017**, *191*, 246–257, doi:https://doi.org/10.1016/j.rse.2017.01.029.
60. Montanaro, M.; Gerace, A.; Lunsford, A.; Reuter, D. Stray Light Artifacts in Imagery from the Landsat 8 Thermal Infrared Sensor. *Remote Sens.* 2014, *6*.
61. Gutman, G.; Ignatov, A. The derivation of the green vegetation fraction from NOAA/AVHRR data for use in numerical weather prediction models. *Int. J. Remote Sens.* **1998**, *19*, 1533–1543.
62. Liang, S. Narrowband to broadband conversions of land surface albedo: I. Algorithms. *Remote Sens. Environ.* **2001**, *76*, 213–238.
63. Talsma, C.J.; Good, S.P.; Jimenez, C.; Martens, B.; Fisher, J.B.; Miralles, D.G.; McCabe, M.F.; Purdy, A.J. Partitioning of evapotranspiration in remote sensing-based models. *Agric. For. Meteorol.* **2018**, *260–261*, 131–143, doi:10.1016/J.AGRFORMET.2018.05.010.
64. Talsma, C.J.; Good, S.P.; Miralles, D.G.; Fisher, J.B.; Martens, B.; Jimenez, C.; Purdy, A.J. Sensitivity of Evapotranspiration Components in Remote Sensing-Based Models. *Remote Sens.* **2018**, *10*, 1601, doi:10.3390/rs10101601.
65. Long, D.; Singh, V.P. Assessing the impact of end-member selection on the accuracy of satellite-based spatial variability models for actual evapotranspiration estimation. *Water Resour. Res.* **2013**, *49*, 2601–2618.
66. Timmermans, W.J.; Kustas, W.P.; Anderson, M.C.; French, A.N. An intercomparison of the surface energy balance algorithm for land (SEBAL) and the two-source energy balance (TSEB) modeling schemes. *Remote Sens. Environ.* **2007**, *108*, 369–384.
67. Long, D.; Singh, V.P.; Li, Z.-L. How sensitive is SEBAL to changes in input variables, domain size and satellite sensor? *J. Geophys. Res. Atmos.* **2011**, *116*, doi:10.1029/2011JD016542.
68. Carlson, T.N. Triangle Models and Misconceptions. *Int. J. Remote Sens. Appl.* **2013**, *3*, 155–158.
69. Sousa, D.; Small, C. Mapping and Monitoring Rice Agriculture with Multisensor Temporal Mixture Models. *Agric. For. Meteorol.*
70. Small, C. Comparative analysis of urban reflectance and surface temperature. *Remote Sens. Environ.* **2006**, *104*, 168–189.
71. Marshall, M.; Thenkabail, P.; Biggs, T.; Post, K. Hyperspectral narrowband and multispectral broadband indices for remote sensing of crop evapotranspiration and its components (transpiration and soil evaporation). *Agric. For. Meteorol.* **2016**, *218–219*, 122–134, doi:https://doi.org/10.1016/j.agrformet.2015.12.025.